

P-type behavior of CrN thin films by control of point defects

Arnaud le Febvrier^{1*}, Davide Gambino^{1*}, Fabien Giovannelli², Babak Bakhit¹, Simon Hurand³, Gregory Abadias³, Björn Alling¹, Per Eklund¹

*Corresponding authors: arnaud.le.febvrier@liu.se, davide.gambino@liu.se

Affiliation

¹ *Department of Physics, Chemistry and Biology (IFM), Linköping University, SE-58183 Linköping, Sweden*

² *GREMAN UMR-CNRS 7347, Université de Tours, INSA Centre Val de Loire 15 rue de la chocolaterie, CS 2903, 41029 Blois Cedex, France*

³ *Institut Pprime, Département de Physique et Mécanique des Matériaux, UPR 3346, CNRS-Université de Poitiers-ENSMA, 11 Boulevard Marie et Pierre Curie, - TSA 41123, 86073 Poitiers Cedex 9, France*

Keywords

Nitride, sputtering, interstitial defects, vacancies, density functional theory (DFT)

Abstract

We report the results of a combined experimental and theoretical study on nonstoichiometric $\text{CrN}_{1+\delta}$ thin films grown by reactive magnetron sputtering on c-plane sapphire, MgO (100) and LaAlO_3 (100) substrates in a Ar/N_2 gas mixture using different percentage of N_2 . There is a transition from n-type to p-type behavior in the layers as a function of nitrogen concentration varying from 48 at. % to 52 at. % in CrN films. The compositional change follows a similar trend for all substrates, with a N/Cr ratio increasing from approximately 0.7 to 1.06-1.10 by increasing percentage of N_2 in the gas flow ratio. As a result of the change in stoichiometry, the lattice parameter and the Seebeck coefficient increase together with the increase of N in $\text{CrN}_{1+\delta}$; in particular, the Seebeck value coefficient transitions from $-50 \mu\text{V.K}^{-1}$ for $\text{CrN}_{0.97}$ to $+75 \mu\text{V.K}^{-1}$ for $\text{CrN}_{1.1}$. Density functional theory calculations show that Cr vacancies can account for the change in Seebeck coefficient, since they push the Fermi level down in the valence band, whereas N interstitial defects in the form of N_2 dumbbells are needed to explain the increasing lattice parameter. Calculations including both types of defects, which have a strong tendency to bind together, reveal a slight increase in the lattice parameter and a simultaneous formation of holes in the valence band. To explain the experimental trends, we argue that both Cr vacancies and N_2 dumbbells, possibly in combined configurations, are present in the films. We demonstrate the possibility of controlling the semiconducting behavior of CrN with intrinsic defects from n- to p-type, opening possibilities to integrate this compound in energy-harvesting thermoelectric devices.

Introduction

Thermoelectric (TE) materials are promising candidates for energy-harvesting devices [1-3] that can convert heat into electricity when they are exposed to a temperature gradient. A thermoelectric device is composed of several legs electrically connected in series of n-type and p-type semiconductors [4,5]. The TE figure of merit (zT), a dimensionless quantity related to the TE efficiency, is defined as $zT = S^2 \sigma T / (k_e + k_p)$, where S , σ , T , k_e and k_p are the Seebeck coefficient, the electrical conductivity, the absolute temperature, the electronic thermal conductivity and lattice thermal conductivity (phonon), respectively. zT can be optimized by maximizing the parameter S^2 , called power factor, and minimizing the lattice thermal conductivity, which is the main contribution to the thermal conductivity in semiconductors. Among established thermoelectric materials, telluride-based materials typically show the highest zT values [3]. However, for future production and/or use in commercial aspect, search for alternative materials is urgently needed because of the scarcity, toxicity, and low global production of tellurium [6-10]. To accommodate this demand, the search for new thermoelectric materials is largely focused on silicides, oxides, nitrides, and organic materials with elements which are more abundant and less toxic [7,11]. Among nitrides for thermoelectric applications, scandium- and chromium-based nitrides have been reported with promising thermoelectric properties [12-18].

Sc- and Cr-based nitride materials exhibit n-type conduction with promising properties for further integration in TE devices. However, for device integration both n-type and p-type materials are needed. P-type ScN can be fabricated by alloying/doping with Mg or Mn on Sc sites [10,13,19]. The power factor of n-type CrN is high, and this material has an intrinsically lower thermal conductivity than ScN [12,20,21]. The main mechanism that leads to lower thermal conductivity in CrN is related to its magnetic properties, since this compound undergoes a transition from an antiferromagnetic to a paramagnetic (PM) state at a critical temperature T_c close to 280 K [22]: above T_c , scattering of phonons due to the magnetic disorder reduces even further the thermal conductivity as compared to other nonmagnetic rock-salt transition-metal nitrides [23].

First-principles modelling of materials in the PM state is not trivial. Approximation of the PM phase of a magnetic material with a nonmagnetic state leads to wrong results in some cases [24-27]. However, the PM phase can be modelled by density functional theory (DFT) calculations with the disordered local moment (DLM) approximation, in which the PM state is represented by disordered magnetic moments in the lattice [28-32]. Initially employed with the coherent potential

approximation (CPA) [33], it has been then extended to supercell calculations [34], which allow to perform local lattice relaxations, a main requisite for the investigation of defects. In the past years, other methods to perform relaxations consistently in the PM state have been also developed [35,36].

Defects are important in transition-metal nitrides with the cubic rock-salt structure, susceptible to non-stoichiometry [15,37-40]. In the case of CrN, the presence of vacancies and/or other types of defects coupled with the narrow band gap of the intrinsic material varies the charge carrier density and thus provides a wide range of electrical properties from semiconductor to metallic-like conduction [41,42].

Several studies have reported that n-type $\text{CrN}_{1-\delta}$ exhibit relatively high zT (0.1 - 0.35 in a temperature range from RT to 400 °C, with moderate electrical conductivity (1.7 – 350 $\text{m}\Omega\cdot\text{cm}$), low thermal conductivity (2 - 4 $\text{W}\cdot\text{m}^{-1}\cdot\text{K}^{-1}$), and high absolute values of the Seebeck coefficient (135 - 200 $\mu\text{V}\cdot\text{K}^{-1}$) [15,43-45]. The n-type behavior of understoichiometric $\text{CrN}_{1-\delta}$ has been explained by DFT calculations to be induced by N vacancies, which shift the Fermi level towards the conduction band [38]. N interstitials in the form of N_2 dumbbells have been also shown to induce an n-type behavior in this compound, although the effect is weaker than observed with N vacancies. McGahay et al. showed that growing CrN thin films in the presence of oxygen leads to the formation of an oxynitride $\text{Cr}_{1-x/2}\text{N}_{1-x}\text{O}_x$ compound with random distribution of O atoms on the N sublattice accompanied by the formation of Cr vacancies [46]. By increasing O concentration, they observed an insulator-to-metal transition, followed by an additional transition back to an insulating state. For $x \leq 0.26$, the $\text{Cr}_{1-x/2}\text{N}_{1-x}\text{O}_x$ layers are n-type semiconductors with increasing number of carriers of this type. On the other hand, p-type behavior was observed for overstoichiometric CrN doped with Al ($\text{Cr}_{0.96}\text{Al}_{0.04}\text{N}_{1.17}$) film [47] and on films deposited by radio-frequency sputtering using relatively large portion of nitrogen as reactive gas, although no detailed film composition was reported in the latter case [48].

With a motivation to develop both n-type and p-type CrN-based thermoelectric materials, ultimately required for TE devices, we demonstrate here the possibility to convert n-type CrN to p-type $\text{CrN}_{1+\delta}$ by controlling the stoichiometry, without the need for dopants. We show the effect of Cr vacancies combined with nitrogen interstitials on the thermoelectric properties of this $\text{CrN}_{1+\delta}$ compound. The different characteristics of the films synthesized by reactive magnetron sputtering were examined (crystal structure, morphology, elemental composition), and the thermoelectric properties evaluated from ambient temperature up to 525 °C. DFT calculations of PM $\text{CrN}_{1+\delta}$ are carried out with defects compatible with the N overstoichiometry on the Cr sublattice, on the N

sublattice, and on both sublattices at the same time. These calculations indicate that Cr vacancies can induce the p-type behavior observed experimentally, although presence of N₂ dumbbells is needed to explain the expansion of the lattice parameter.

Experimental and method

Material synthesis:

330 nm CrN_{1+δ} thick films were deposited simultaneously onto c-plane sapphire, MgO (100) and LaAlO₃(100) (abbreviated LAO) substrates using a magnetically unbalanced magnetron sputtering system (base pressure $\sim 10^{-5}$ Pa) equipped with confocal target configuration [49]. The Cr (99.95 % purity) target was 7.5-cm (3 inch) diameter water-cooled disk electrically connected to a DC power supply at a constant power of 200 W. The films were deposited using different N₂/Ar gas mixtures. The flow of nitrogen was kept constant at 20 sccm, while the flow of argon was changed from 6 to 30 sccm leading to different N₂/Ar gas-flow ratios from 79 % to 40 % and different working pressures from 0.25 to 0.40 Pa, respectively. The target was located at 18 cm from the substrate, which was mounted on a rotating sample holder coupled with a heating element. The nominal temperature was fixed at T_s = 700 °C (corresponding approximately to 600°C at the substrate surface), and a substrate bias voltage of -30 V (DC equivalent) was applied during deposition using an RF power supply. The substrates were first cleaned using detergent steps, then 10 min using acetone in ultrasonic bath and repeated with ethanol and finally blown dry with a N₂-gun. The detergent steps are described elsewhere [50]. Prior deposition, an in-situ Ar etching was performed using a RF substrate bias of – 90 V for 2 minutes. The total deposition time was 3500 s.

Materials analysis:

The crystal structure of the films was determined by X-ray diffraction (XRD). The θ -2 θ scans were recorded in an X'Pert PRO from PANalytical in a Bragg Brentano using a Cu K α radiation with a nickel filter. Philips X'Pert-MRD with Cu K α radiation was used determining with accuracy the cell parameter on MgO substrate using a hybrid mirror on the incidence beam path and a triple axis Ge 220 analyser on the diffracted beam path. The surface morphology of the films was examined using a scanning electron microscope (SEM, LEO Gemini 1550, Zeiss) operated at 5 KeV.

The elemental compositions of nitride films were determined by time-of-flight elastic recoil detection analysis (ToF-ERDA) in a tandem accelerator. ToF-ERDA was carried out with a 36 MeV $^{127}\text{I}^{8+}$ probe beam incident at 67.5° with respect to the sample surface normal, and recoils are detected at 45°. More details about the measurements are given in reference [51]. The elemental compositions were also determined using a wavelength dispersive spectrometer (WDS) unit from Oxford Instruments (High Wycombe, UK) attached to a JEOL 7001 TTLS scanning electron microscope (Tokyo, Japan) operated at 10 kV.

Several measurement setups were used to investigate the electrical and thermoelectric properties. The Seebeck coefficient was measured using two different setups. The first one at room temperature (RT) using a home-built thermoelectric measurement setup equipped with two Peltier heat sources for creating a temperature gradient in the sample, two K-type thermocouples for measuring the temperature. The two electrodes are made of Cu and are in contact with the sample in an area of 9 mm x 1mm in which the K-type thermocouples are present and electrically isolated. The different voltages obtained for different ΔT (0 to 10 K) were measured with a Keithley 2001 multimeter and two thermometers. Room temperature resistivity measurements were performed in a Van der Pauw configuration using a Ecopia AMP-55 Hall measurement system. The in-plane Seebeck coefficient and the electrical resistivity were measured simultaneously under a low-pressure helium atmosphere (~ 0.09 MPa, purity 99.999 ($\text{H}_2\text{O} < 3\text{ppm}$ and $\text{O}_2 < 2\text{ppm}$)) using ULVAC-RIKO ZEM3 from RT up to 400 °C. The substrate contribution to the Seebeck coefficient and electrical resistivity is negligible, and the instrumental error is within 10 %.

Theoretical calculation:

Density functional theory (DFT) calculations were performed with the Vienna Ab initio Simulation Package (VASP) [52,53] with projector augmented-wave (PAW) [54,55] potentials and employing LDA exchange-correlation functional. Strong electron correlation was included with the LDA+U scheme as devised by Dudarev [56], employing a value $U^{\text{eff}} = 3$ eV on the Cr 3d electrons which is known to describe well both the low and high temperature phases, together with reasonable electronic properties [34]. The energy cut-off for expansion of plane-waves was set to 400 eV, while sampling the first Brillouin zone with a $3 \times 3 \times 3$ Monkhorst-Pack k -mesh. The criterion for convergence of electronic optimization was set to 10^{-3} eV/supercell. Spin-polarized calculations are carried out with collinear moments. To model the PM phase, we used the magnetic sampling method (MSM)

[34], a supercell implementation of the DLM approach, which consists of employing many different magnetic configurations of randomly distributed up and down moments. The defective $\text{CrN}_{1+\delta}$ structures were relaxed in the DLM state with the DLM-relaxation method described in Ref. [35] using the defect free equilibrium volume.

The equilibrium lattice parameter of the structures with a single defect (a Cr vacancy or a N_2 dumbbell) was obtained from the equation of state, calculated with a supercell made of $2 \times 2 \times 2$ repetitions of the conventional rock-salt cell (32 formula units) and employing five different volumes, using the atomic positions relaxed at the defect-free equilibrium volume. At each volume, we carried out MSM calculations with ten different magnetic configurations. The equation of state was calculated for each magnetic configuration separately and the equilibrium lattice parameter for the defective structures was then retrieved as an average of the equilibrium lattice parameters of each magnetic configuration. For the combined defects (Cr vacancy and N_2 dumbbell in the same supercell), we performed the same procedure but with a $3 \times 3 \times 3$ supercell.

The calculation of formation and interaction energy of defects was carried out with a $3 \times 3 \times 3$ supercell ($n = 108$ formula units) to minimize self-interaction of the defects. The energy of the defective supercells was obtained by MSM static calculations with 25 different magnetic configurations on the geometry resulting from DLM-relaxation of these $3 \times 3 \times 3$ supercells. The total energy of the supercell was obtained as an average over all the magnetic configurations. The formation energy of the single or combined defect is defined as:

$$E^f(\text{Cr}_{n-\nu}\text{N}_{n+d}) = E(\text{Cr}_{n-\nu}\text{N}_{n+d}) - \left[\frac{n-\nu}{n} E(\text{Cr}_n\text{N}_n) + \frac{\nu+d}{2} E(\text{N}_2) \right], \quad (1)$$

where $E(\text{Cr}_{n-\nu}\text{N}_{n+d})$ is the energy of the defective supercell, $E(\text{Cr}_n\text{N}_n)$ is the energy of the defect-free CrN $3 \times 3 \times 3$ supercell, n is the number of formula units in the defect-free supercell, $E(\text{N}_2)$ is the energy of a N_2 molecule, $\nu = \{0,1\}$ is an index that indicates the presence ($\nu = 1$) or absence ($\nu = 0$) of a vacancy in the Cr sublattice, and $d = \{0,1\}$ is a corresponding index for the N interstitial atom in the form of a N_2 dumbbell (notice the different sign for the ν and d indices in the formula). We choose to employ the chemical potential of N for both types of defects because this is likely the relevant chemical potential in experiments [57]. The interaction energy between two defects is defined as:

$$E^i(\text{Cr}_{n-\nu}\text{N}_{n+d}) = E^f(\text{Cr}_{n-\nu}\text{N}_{n+d}) - E^f(\text{Cr}_{n-\nu}\text{N}_n) - E^f(\text{Cr}_n\text{N}_{n+d}), \quad (2)$$

with negative (positive) energy indicating attractive (repulsive) interaction.

In addition, we calculated the density of state (DOS) of relevant supercells with defects in the PM phase as an average over all MSM magnetic configurations employed.

Results and discussion

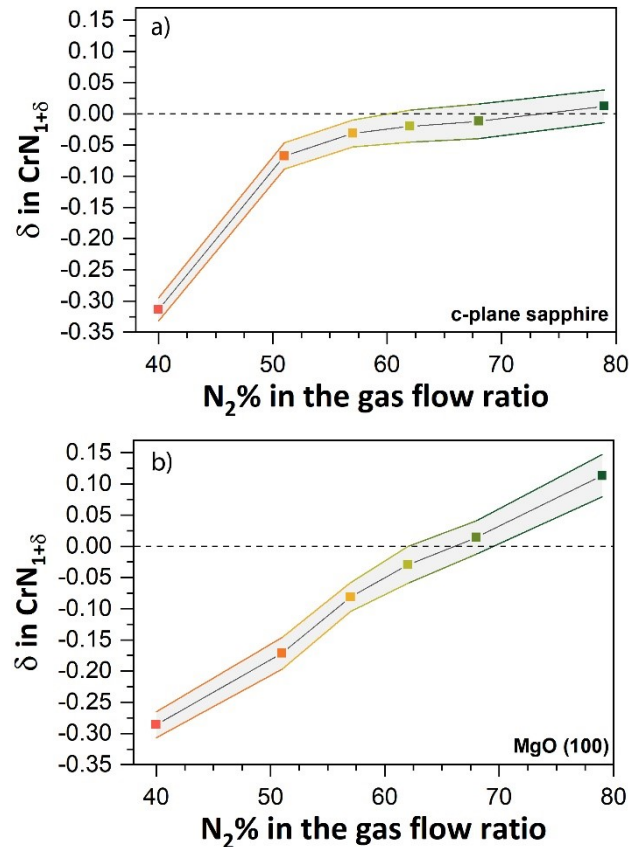


Figure 1: Film composition (from ToF-ERDA) represented as CrN_{1+δ} for the series of film deposited on c-plane sapphire (a) and MgO (100) (b) with different N₂/Ar gas flow ratio. The grey zone represents the error bar of the ToF-ERDA analysis. Note here that the oxygen contamination is not taken into account in the calculation.

Figure 1 is a visual representation of the evolution of the film composition, denoted as CrN_{1+δ}, measured by ToF-ERDA on c-plane sapphire and MgO (100) when the N₂% in the gas flow is varied. For all samples, the oxygen contamination in the films was estimated to be equal or less than 0.9 % (table S1 in the supplementary information). The N/Cr ratio in the films increases by increasing the N₂/Ar gas flow ratio during deposition. On all substrates and at low N₂%, the films have the N/Cr ratio ≈ 0.7 , which increases to values higher than 1.0 (between 1.01 and 1.11 depending on the substrate) when the N₂% increases. Although the films were deposited on the different substrates in the same batch, differences in elemental composition are observed between substrates. For example, the films

on MgO (100) have a higher N/Cr ratio in the N-rich side of the series and a larger decrease in the N/Cr ratio is found when decreasing N₂/Ar flow ratio in comparison with the films deposited on c-plane sapphire. Within the error bar of the ToF-ERDA data analysis, the films deposited on c-plane sapphire at a N₂% between 57 and 77% can be considered stoichiometric (CrN₁). Nevertheless, small differences are present with the nominal value varying from CrN_{0.97} to CrN_{1.01} when the films are deposited at 57 or 77 N₂%. The films deposited using 51 N₂% or less are understoichiometric with a minimum value of δ in CrN_{1+ δ} at -0.32 (or CrN_{0.68}). On MgO (100), the films deposited between 62 and 68 N₂% are stoichiometric (CrN₁). The films deposited using 57 N₂% or less are understoichiometric with a minimum value of δ in CrN_{1+ δ} at -0.29 (or CrN_{0.71}). Note here that the measurements were performed using two different techniques which their results show good agreement. The details of the elemental composition analysis can be found in the supplementary information (table S1 and table S2). The oxygen content detected (1% or less) was not included in the calculation of the ratio anion/cation in the NaCl structure of CrN (Fig. 1). If the oxygen was included in the calculation, all ratios Anion/Cr would increase by an average of + 0.02 in the N-rich side of the series: for example, at the highest N₂% and on MgO (100), the (N+O)/Cr becomes 1.13 instead of 1.11 without taking into account the oxygen.

The morphology of the films in the N-rich CrN_{1+ δ} is similar within a given substrate series, with rounded triangular grains which tend to merge, forming elongated features on c-plane sapphire while a well-arranged pavement of square shaped grains is observed on MgO (100) and LAO (100) when the N₂% is higher than 57%. The changes on c-plane sapphire are relatively small compared to the other substrates and explained by the relatively small changes in the composition in the films. An overstoichiometric film (deposited with 68 % and 77 % of N₂) seems to consist of smaller grains than an understoichiometric film (deposited with 57 % of N₂). More details on the morphology are presented in the supplementary information (Fig. S3).

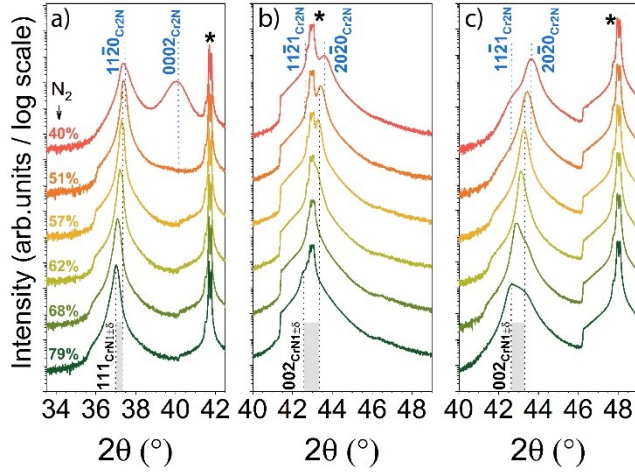


Figure 2: XRD patterns of $\text{CrN}_{1+\delta}$ films deposited using different $\text{N}_2\%$ in the gas flow ratio (from 40 to 77 %) and on a) c-plane Al_2O_3 , b) MgO (100), c) LAO (100). Measurement performed in a Bragg Brentano configuration using a $\text{Cu K}\alpha$ radiation with a nickel filter. Peaks marked with * correspond to the substrate peaks: 0006 (Al_2O_3), 200 (MgO), 200 (LAO)

Figure 2 shows the XRD patterns of the $\text{CrN}_{1+\delta}$ films deposited using different $\text{N}_2\%$ in the gas flow ratio and on different substrates (c-plane sapphire, MgO (100) and LAO (100)). The full XRD patterns ($2\theta: 10\text{--}90^\circ$) are presented in the supplementary information (Fig. S1). Regardless of the substrate, the diffractogram of the films deposited at 72 % N_2 in the gas flow ratio exhibits one diffraction peak belonging to the film depending on the $\text{N}_2\%$ in the gas flow. This peak is identified as the one from the rock-salt CrN phase. Note here that the diffraction peak belonging to the film differs between 111 and 002, revealing a highly oriented film along the [111] or [001] directions of CrN on c-plane sapphire or on LAO (100) and on MgO (100), respectively. The orientation observed on c-plane sapphire is typical of an epitaxial growth which consists of twin domains in the cubic material thin film on c-plane sapphire [58]. On MgO (100) and LAO (100) substrates, CrN grows following the so-called cube-on-cube epitaxial growth [59,60]. The term “epitaxial” is here used to describe the polycrystalline film are composed of grains epitaxially oriented to the substrate crystal structure. Note here that the orientation of the films is consistent with the morphology of the N-rich $\text{CrN}_{1+\delta}$ films with triangular shape grains for a (111) oriented films and square shape grains for (001) oriented films. The orientation of the films, hence the surface energy, may influence the adsorption/reaction of nitrogen molecules on top the surface of the film during deposition. This influence seems to be more pronounced for (001) oriented films than for (111) oriented ones, as Figure 1 shows.

At lower $\text{N}_2\%$ in the gas flow ratio (51 %), two other diffraction peaks are visible on c-plane sapphire at $2\theta = 37.4^\circ$ and 40.6° identified as the 1120 and 0002 peak from Cr_2N phase, see Fig. 2(a).

These peaks are clearly visible on the XRD pattern for the film deposited at 40 % of N₂, but can be also distinguished from an increase in the background intensity and a different shape of the peak on the XRD pattern for the film deposited at 51 % of N₂. For the series deposited on MgO, this secondary phase identified as Cr₂N is not clearly visible on a Bragg Brentano configuration measurement due to the high intensity of the substrate peak, Fig. 2(b). A 0-2θ measurement using a monochromatic Cu K_{α1} and an ω offset of 0.1° allows to diminish the intensity of the 002 peak from MgO and identify the phases present in the film (Fig. S2 in supplementary information). Similarly to the films deposited on c-plane sapphire, the phase composition in the films varies from pure CrN_{1+δ} at high N₂% to a mixture of CrN_{1+δ} and Cr₂N when the N₂% is reduced at 51%. At the lowest amount of N₂% in the gas flow ratio, the film is mainly composed of Cr₂N phase. On all substrates and upon increasing of N₂% in the plasma, the CrN_{1+δ} peak position is shifted towards lower 2θ values. Therefore, increasing nitrogen in CrN_{1+δ} leads to an increase of the cell parameter. Note here that the observations on LAO (100) substrates are similar to the ones on MgO (100) substrates; having the same crystallographic orientation, similar composition and shifts of the diffraction peak when the N₂% in the gas low ratio is changed.

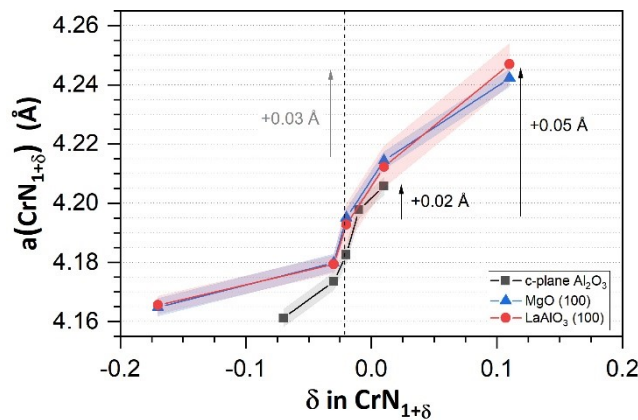


Figure 3: Cell parameter of cubic CrN_{1+δ} phase for films deposited on c-plane Al₂O₃, MgO (100), and LaAlO₃ (100). Values are extracted from the XRD peak corresponding to the main peak of CrN (001 or 111) depending on the substrate (see Fig. 1). The vertical line corresponds to the transition from negative to positive Seebeck coefficient (see Fig. 4). The vertical arrows represent either the change of cell parameter compared to transition from negative to positive Seebeck coefficient and the change between cell parameter for CrN_{1.01} to CrN_{1.13}.

Figure 3 displays the evolution of the cell parameter of the cubic CrN_{1+δ} phase for the different films as a function of δ. Regardless of the substrate used, the CrN_{1+δ} phase has an increase of its cell

parameter when the nitrogen content in the film increases. The stoichiometric film has a cell parameter around 4.20 (± 0.05) Å on all substrates which is comparable to the values reported in literature between 4.15 to 4.18 Å for CrN[43,45,60]. The variation of the cell parameter is dependent of the nitrogen content in the film. A variation of $\delta = + 0.01$ in $\text{CrN}_{1+\delta}$ lead to an increase of the cell parameter of +0.02 Å (+ 0.5%) compared to the stoichiometric CrN. An increase of 1.2% of the cell parameter is observed for an increase of δ to + 0.11 in $\text{CrN}_{1+\delta}$.

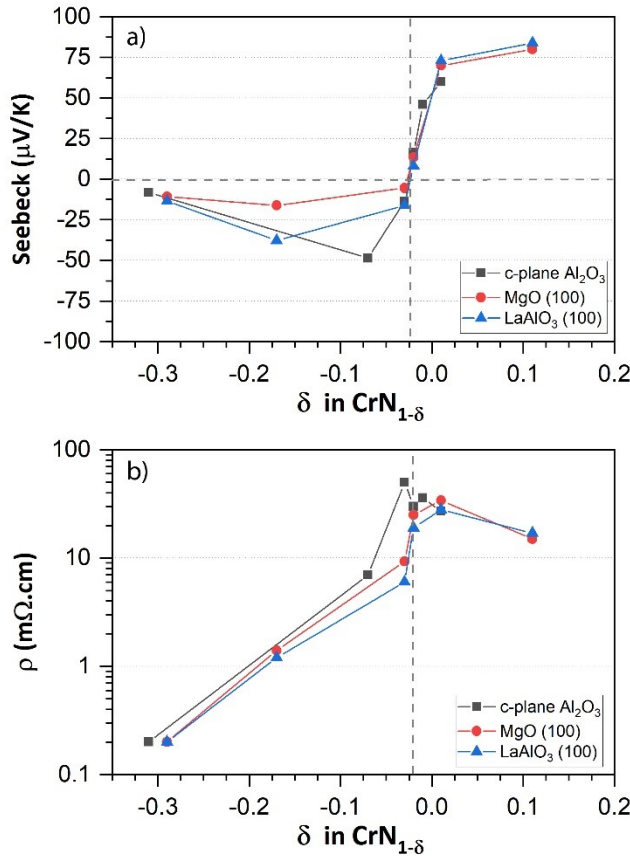


Figure 4: a) Seebeck coefficient RT and b) electrical resistivity values of the films deposited under different N₂% in the gas flow ratio on different substrates (c-plane Al_2O_3 , MgO (100) and LaAlO₃ (100)). The electrical properties are represented versus the nitrogen composition in $\text{CrN}_{1+\delta}$. The vertical line corresponds to the transition from negative to positive Seebeck coefficient.

Figure 4 displays the RT values of the Seebeck coefficient and the resistivity versus the nitrogen composition as δ in $\text{CrN}_{1+\delta}$. Regardless of the substrate, a trend is noticeable for the electrical properties of the film depending on the nitrogen content. The measured Seebeck coefficient at RT is positive (+ 50 to +80 $\mu\text{V.K}^{-1}$) when the films are overstoichiometric and becomes negative (- 25 to -50 $\mu\text{V.K}^{-1}$) when the films are understoichiometric. The transition from positive to negative Seebeck coefficient occurs at δ ≈ -0.03 and not δ = 0, which can be due to the presence of

oxygen contamination (< 1%) and/or experimental uncertainties [46]. The electrical resistivity of the films stays relatively high, between 10 to 80 $\text{m}\Omega\text{.cm}$, for the overstoichiometric films and reduces by one or two orders of magnitude for the understoichiometric ones. The films with $\delta = -0.30$ have a low Seebeck coefficient ($12 \mu\text{V.K}^{-1}$) and low electrical resistivity ($200 \mu\text{}\Omega\text{.cm}$), consistent with the physical characteristics of Cr_2N [61].

Figure 5 represents the thermoelectric properties measurements (Seebeck coefficient and electrical resistivity) from RT to 400°C for the films deposited on c-plane sapphire and on $\text{MgO} (100)$. The trend of the Seebeck coefficient and the electrical resistivity within a substrate series is similar as the one observed on Figure 4 where the measurement was performed on a different setup and only at RT. With the exception of the film with $\delta = -0.30$, the electrical resistivity of the films decreases when the temperature increases revealing semiconductor behavior. The $\text{CrN}_{1+\delta}$ films with $\delta = -0.30$ (corresponding to $\text{CrN}_{0.7}$) have their electrical resistivities increasing when the temperature increases; hence, a metallic behavior with a relatively low resistivity ($0.2 \text{ m}\Omega\text{.cm}$) consistent with the properties of Cr_2N [61]. On both substrates, the Seebeck coefficient values tend to increase up to a maximum attained around $200\text{--}250^\circ\text{C}$ and then decreases slowly. Note that the film with δ of $+0.11$ on $\text{MgO} (100)$ exhibits higher Seebeck coefficient values, and a maximum is observed at higher temperature (350°C) compared to the other films.

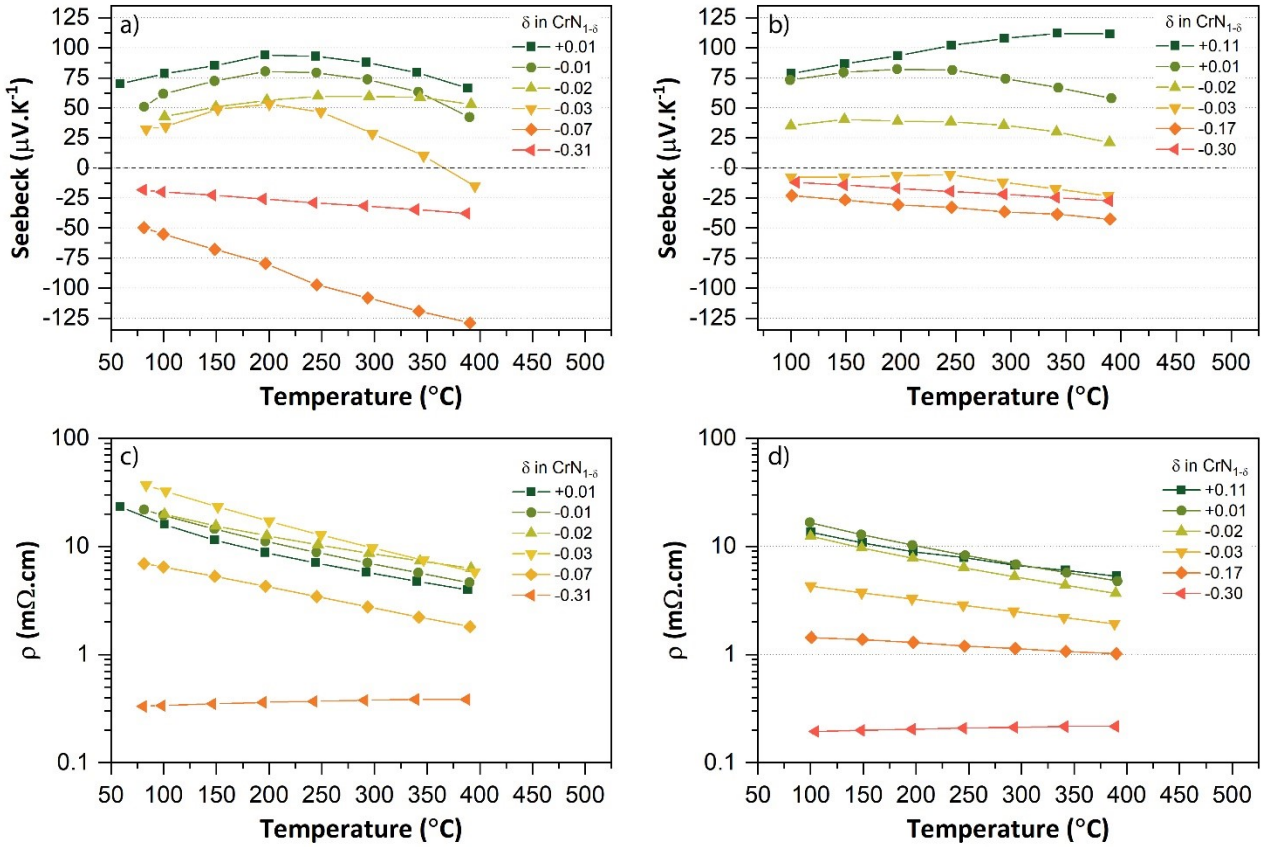


Figure 5: Temperature-dependence of the Seebeck coefficient (a, b) and electrical resistivity (c, d) of the films with different compositions: a) and c) on c-plane Al₂O₃, b) and d) on MgO (100)

The Seebeck coefficient of semiconductors can be described by the Mott-Boltzmann formalism from a relatively simple model with energy-independent scattering approximation and parabolic band [4]. The Seebeck coefficients (S_n) for the majority and minority charge carriers are defined as followed:

$$S_n = \frac{8\pi^2 k_B^2 T}{3e\hbar^2} m^* \left(\frac{\pi}{3n}\right)^{2/3} \quad (3)$$

where n corresponds to the carrier concentration of electron (or p for holes), m^* is the effective mass, T the temperature and \hbar is Planck's constant [4,5]. For intrinsic semiconductors, both conduction and valence bands may play a role in the transport. Thus, the total Seebeck (S_T) coefficient is given by [5]:

$$S_T = \frac{S_n \sigma_n + S_p \sigma_p}{\sigma_n + \sigma_p} \quad (4)$$

The charge carriers (electrons (n) and holes (p)) would then compete and cancel out the induced Seebeck voltage. This is in analogy with metals, which have low Seebeck coefficients, and an extreme case is Ti₃SiC₂ with $S = 0$ over a wide temperature range [62-64]. In the present case, both

p-type and n-type behavior were observed depending on the composition with a transition at room temperature happening at $\delta = -0.03$ in $\text{CrN}_{1-\delta}$. The temperature evolution of the Seebeck coefficient values for samples having low absolute Seebeck values ($\delta \approx -0.03$) can come from more complex phenomena with variation of both types of charge carriers (electrons and holes) with respect to both concentrations and mobilities when the temperature increases.

A theoretical approach was used to understand the underlying cause of this transition in the Seebeck values from negative to positive or from n-type to p-type semiconductor behavior as a function of the nitrogen content. DFT calculations were used to compute the formation energy of some possible defects responsible for nitrogen overstoichiometry in cubic $\text{CrN}_{1+\delta}$ phase. The defects considered are the Cr vacancy, the N interstitial, and the N antisite. The N interstitial defect in CrN has been previously [38] shown to be most stable in a dumbbell configuration, i.e., a N_2 dimer placed with its center on a lattice site and aligned along a $\langle 111 \rangle$ direction. The formation energies of these defects are reported in Table 1. Cr vacancy is found to have the lowest formation energy of 2.48 eV. Formation energies in general define the relative stability of different defects in equilibrium conditions; however, the deposition technique employed in this study is far from equilibrium; therefore, thermodynamic reasoning alone cannot establish the prevalence of one defect over the other in the as-deposited films. For this reason, we cannot rule out the presence of both Cr vacancies and N dumbbells. Calculations with a combination of Cr vacancy and N_2 dumbbells were also taken into account, and we observe that the formation energy of these complexes is generally lower than the N antisite (see Table 1), which we therefore neglect in the rest of the discussion. We consider four configurations of Cr vacancy + N_2 dumbbell defects, which are shown in Fig. 6: in the first two cases [a) and b) in Fig. 6], the dumbbell is positioned on a lattice site nearest neighbor to the Cr vacancy, and aligned either along [110] in Fig. 6a) or [100] in Fig. 6b). In the third and fourth configurations (Fig 6c and 6d), the N_2 dumbbell is in third nearest neighbor position to the Cr vacancy with different orientations, where in the former case the dumbbell is oriented toward the vacancy. As Table 1 shows, the formation energy depends on the defect configuration, with energy of formation varying from 4.75 to 6.07 eV. The combined defect with highest formation energy displays a weak interaction energy as compared to the other defects, as can also be realized from Fig. 6d), since in this case the dumbbell is not directed towards the Cr vacancy. Finally, we see that the interaction energies of the defects are all negative, indicating attraction between the Cr vacancy and

N_2 dumbbell; therefore, during the deposition process, we can argue that if these defects are formed near each other, they will attract and form a more stable configuration.

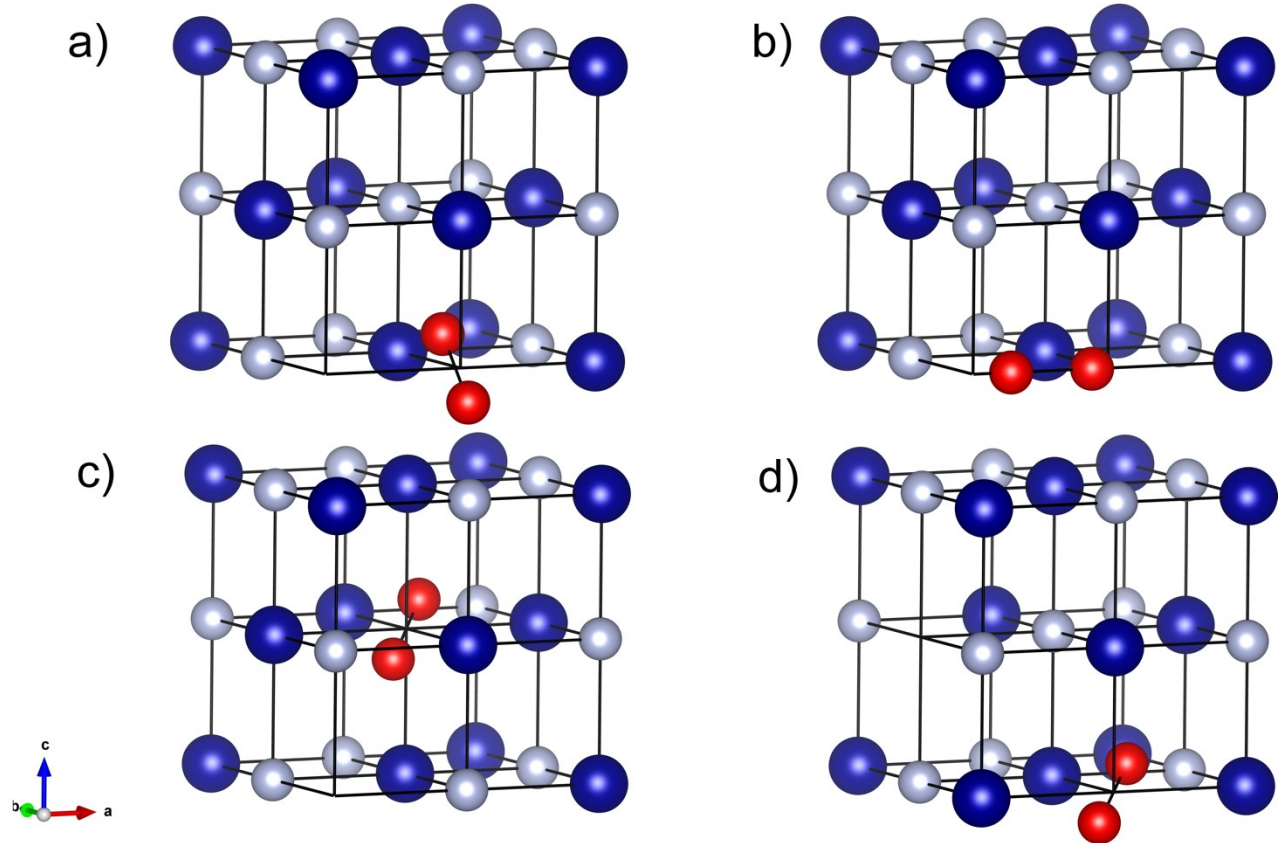


Figure 6: Structural models of the combined defects Cr vacancy- N_2 dumbbell in a single conventional rock-salt cell. Cr atoms are in blue, N atoms in grey and the N atoms in the dumbbell in red. Notice the missing Cr atom in position (0,0,0) in all models except in d), where the vacancy is at (0,1/2,1/2). The atoms on ideal lattice positions are shown without relaxation, whereas the N_2 dumbbell is shown as relaxed. From a) to d), the N_2 dumbbell is oriented in directions [110], [100], [111] and [111], respectively.

Table 1: Formation energy of the Cr vacancy (Cr^v), N_2 dumbbell (N_2^d), and N antisite (N^a) defects, and interaction energies of combined Cr vacancy and N_2 dumbbell ($Cr^v + N_2^d$) defects in the different configurations shown in Fig. 7. For the combined defects, the notation (a), (b), (c) and (d) refers to Fig. 6.

Type of defects	Formation energy (eV)	Interaction energy (eV)
Cr^v	2.48	-
N_2^d	3.61	-
N^a	6.91	-
$Cr^v + N_2^d$ (a)	4.75	- 1.34
$Cr^v + N_2^d$ (b)	5.23	- 0.86

$\text{Cr}^v + \text{N}_2^d$ (c)	5.88	- 0.21
$\text{Cr}^v + \text{N}_2^d$ (d)	6.07	- 0.02

Table 2: Equilibrium lattice parameter for defect-free CrN, CrN with one Cr vacancy ($\text{CrN}_{1.03}$), and with one N_2 dumbbell ($\text{CrN}_{1.03}$). Note here that a supercell made of 2'2'2 or 3x3x3 repetitions of the conventional rock-salt cell is used for the single defect or the combined defect calculation, respectively.

Type of defects	Labeled	N/Cr	Lattice parameter (Å)	Relative change (%)
Defect free	CrN	1.00	4.129	0
Cr^v	Cr_{1-x}N	1.03	4.118	- 0.3
N_2^d	CrN_{1+y}	1.03	4.159	+ 0.7
$\text{Cr}^v + \text{N}_2^d$ (a)	$\text{Cr}_{1-x}\text{N}_{1+y}$	1.02	4.136	+ 0.2

Table 2 reports the computed equilibrium lattice parameters for defective (Cr vacancy and the N_2 dumbbell and the most stable configuration of the combined defect) and defect-free CrN cubic structures. Comparatively to the defect-free structure, it is found that the N_2 dumbbell leads to an expansion of 0.7% of the lattice parameter, whereas the Cr vacancy induces a reduction by 0.3%; however, the combined defect seems to lead to a small increase of the lattice parameter as well, consistent with the experimental results with a variation of + 0.5 to + 1.2 %.

From previous studies [38], it is known that N vacancies in CrN can induce n-type behavior in the DOS. The same behavior is argued for in the case of the N_2 dumbbell, although with a much weaker strength. Figure 7 displays the DOS for the single defects and for the most stable configuration with the two defects combined [figure 6a)]. We see that in the present cases with the Cr vacancy, the valence band is shifted to higher energy, leading to a p-type behavior, as observed in the present experiments. The N_2 dumbbell alone affects the DOS very weakly, shifting the valence band to lower energies as compared to the defect free system, whereas the Cr vacancy shows a more pronounced effect on the shift of the same band. The combination of the two defects is somewhat in between, but with character more similar to the Cr vacancy. These results indicate that the N_2 dumbbells alone, which can account for expansion of the lattice parameter as a function of N_2 content in the plasma, cannot be responsible for the p-type behavior seen in the experiments, but a

combination of N_2 dumbbells and Cr vacancies could instead account for the positive Seebeck coefficient together with an expanded lattice parameter. It is also possible that more complex defects could lead to even larger effects on the electronic structure; however, the main players in these complexes would arguably be the Cr vacancy and the N_2 dumbbell.

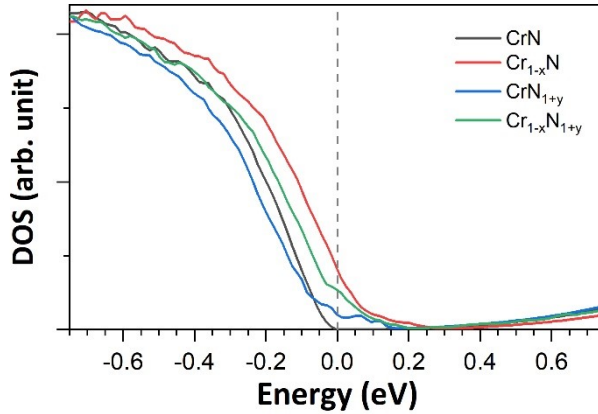


Figure 7: Electronic DOS around the Fermi level calculated with DFT on defect-free CrN, CrN with a Cr vacancy ($Cr_{1-x}N$), CrN with a N_2 dumbbell (CrN_{1+y}), and with the most stable configuration of the combined defects ($Cr_{1-x}N_{1+y}$), shown in Fig. 6a). The zero of the energy is the Fermi level.

Conclusion

In conclusion, we show the possibility of synthesizing nonstoichiometric $CrN_{1+\delta}$ thin films ranging from n- to p-type behavior by increasing the N content. We explain this behavior with first principles calculations of intrinsic defects, which show that Cr vacancies induce the p-type behavior and N_2 dumbbells increase the lattice parameter, as observed in experiments. These two defects also show a strong interaction energy, suggesting that they attract each other and form complexes of defects in the system. Temperature-dependent measurements show also that the overstoichiometric $CrN_{1.11}$ films retain their large positive value of the Seebeck coefficient up to 400°C. This study is important for the development of thermoelectric devices based on CrN without the need of doping with foreign elements.

Acknowledgements

The authors acknowledge support from the Knut and Alice Wallenberg Foundation through the Wallenberg Academy Fellows program (grant no. KAW 2020.0196), the Swedish Research Council (VR) under project grants 2016-03365 and 2021-03826, the Swedish Government Strategic Research Area in Materials Science on Functional Materials at Linköping University (Faculty Grant SFO-Mat-LiU No. 2009 00971), and the Swedish Energy Agency under project 46519-1. The authors also acknowledge support from the Swedish research council VR-RFI (2019-00191) for the Accelerator based ion-technological center and from the Swedish Foundation for Strategic Research (contract RIF14-0053) for the tandem accelerator laboratory in Uppsala University. BA acknowledge funding from the Swedish Foundation for Strategic Research through the Future Research Leaders 6 program, Grant No. FFL 15-0290, from the Swedish Research Council (VR) through Grant No. 2019-05403, and from the Knut and Alice Wallenberg Foundation (Wallenberg Scholar Grant No. KAW-2018.0194). The computations were enabled by resources provided by the Swedish National Infrastructure for Computing (SNIC) at NSC partially funded by the Swedish Research Council through Grant Agreement No. 2018-05973

References

- [1] F. J. DiSalvo, *Science* **285**, 703 (1999).
- [2] J. P. Heremans, M. S. Dresselhaus, L. E. Bell, and D. T. Morelli, *Nat Nano* **8**, 471 (2013).
- [3] X. Zhang and L.-D. Zhao, *J. Materomics* **1**, 92 (2015).
- [4] G. J. Snyder and E. S. Toberer, *Nat Mater* **7**, 105 (2008).
- [5] H. J. Goldsmid, *Introduction to Thermoelectricity* (Springer, Veralg-Berlin Heidelberg, 2010), Mater. Sci.
- [6] M. W. Gaultois, T. D. Sparks, C. K. H. Borg, R. Seshadri, W. D. Bonificio, and D. R. Clarke, *Chem. Mater.* **25**, 2911 (2013).
- [7] J. He, Y. Liu, and R. Funahashi, *J. Mater. Res.* **26**, 1762 (2011).
- [8] P. V. Burmistrova, J. Maassen, T. Favaloro, B. Saha, S. Salamat, Y. Rui Koh, M. S. Lundstrom, A. Shakouri, and T. D. Sands, *J. Appl. Phys.* **113**, 153704 (2013).
- [9] M. Zebarjadi, Z. Bian, R. Singh, A. Shakouri, R. Wortman, V. Rawat, and T. Sands, *J. Electron. Mater.* **38**, 960 (2009).
- [10] B. Saha, M. Garbrecht, J. A. Perez-Taborda, M. H. Fawey, Y. R. Koh, A. Shakouri, M. Martin-Gonzalez, L. Hultman, and T. D. Sands, *Appl. Phys. Lett.* **110**, 252104 (2017).
- [11] G. Kieslich, G. Cerretti, I. Veremchuk, R. P. Hermann, M. Panthöfer, J. Grin, and W. Tremel, *Phys. Status Solidi A* **213**, 808 (2016).
- [12] P. Eklund, S. Kerdsongpanya, and B. Alling, *J. Mater. Chem. C* **4**, 3905 (2016).
- [13] S. Kerdsongpanya, B. Alling, and P. Eklund, *Phys. Rev. B* **86**, 195140 (2012).
- [14] S. Kerdsongpanya, N. V. Nong, N. Pryds, A. Žukauskaitė, J. Jensen, J. Birch, J. Lu, L. Hultman, G. Wingqvist, and P. Eklund, *Appl. Phys. Lett.* **99**, 232113 (2011).
- [15] C. X. Quintela, J. P. Podkaminer, M. N. Luckyanova, T. R. Paudel, E. L. Thies, D. A. Hillsberry, D. A. Tenne, E. Y. Tsymbal, G. Chen, C.-B. Eom, and F. Rivadulla, *Adv. Mater.* **27**, 3032 (2015).
- [16] C. X. Quintela, F. Rivadulla, and J. Rivas, *Appl. Phys. Lett.* **94**, 152103 (2009).
- [17] A. S. Botana, V. Pardo, and W. E. Pickett, *Phys. Rev. Appl.* **7**, 024002 (2017).
- [18] N. Tureson, N. V. Nong, D. Fournier, N. Singh, S. Acharya, S. Schmidt, L. Belliard, A. Soni, A. I. Febvrier, and P. Eklund, *J. Appl. Phys.* **122**, 025116 (2017).
- [19] H. A. AL-Britten, H. Yang, and A. R. Smith, *J. Appl. Phys.* **96**, 3787 (2004).
- [20] M. A. Gharavi, D. Gambino, A. le Febvrier, F. Eriksson, R. Armiento, B. Alling, and P. Eklund, *Materials Today Communications* **28**, 102493 (2021).
- [21] B. Biswas, S. Chakraborty, O. Chowdhury, D. Rao, A. I. K. Pillai, V. Bhatia, M. Garbrecht, J. P. Feser, and B. Saha, *Phys. Rev. Materials* (2021).
- [22] L. M. Corliss, N. Elliott, and J. M. Hastings, *Phys. Rev.* **117**, 929 (1960).
- [23] I. Stockem, A. Bergman, A. Glensk, T. Hickel, F. Körmann, B. Grabowski, J. Neugebauer, and B. Alling, *Phys. Rev. Lett.* **121**, 125902 (2018).
- [24] F. Rivadulla, M. Bañobre-López, C. X. Quintela, A. Piñeiro, V. Pardo, D. Baldomir, M. A. López-Quintela, J. Rivas, C. A. Ramos, H. Salva, J.-S. Zhou, and J. B. Goodenough, *Nature Materials* **8**, 947 (2009).
- [25] B. Alling, T. Marten, and I. A. Abrikosov, *Nature Materials* **9**, 283 (2010).
- [26] J. Varignon, M. Bibes, and A. Zunger, *Nat. Commun.* **10**, 1658 (2019).
- [27] F. Körmann, A. Dick, B. Grabowski, T. Hickel, and J. Neugebauer, *Phys. Rev. B* **85**, 125104 (2012).
- [28] J. Hubbard, *Phys. Rev. B* **19**, 2626 (1979).
- [29] J. Hubbard, *Phys. Rev. B* **20**, 4584 (1979).
- [30] J. Hubbard, *Phys. Rev. B* **23**, 5974 (1981).
- [31] H. Hasegawa, *J. Phys. Soc. Jpn.* **46**, 1504 (1979).
- [32] H. Hasegawa, *J. Phys. Soc. Jpn.* **49**, 178 (1980).
- [33] B. L. Gyorffy, A. J. Pindor, J. Staunton, G. M. Stocks, and H. Winter, *Journal of Physics F: Metal Physics* **15**, 1337 (1985).
- [34] B. Alling, T. Marten, and I. A. Abrikosov, *Phys. Rev. B* **82**, 184430 (2010).
- [35] D. Gambino and B. Alling, *Phys. Rev. B* **98**, 064105 (2018).

[36] O. Hegde, M. Grabowski, X. Zhang, O. Waseda, T. Hickel, C. Freysoldt, and J. Neugebauer, *Phys. Rev. B* **102**, 144101 (2020).

[37] L. Tsetseris, N. Kalfagiannis, S. Logothetidis, and S. T. Pantelides, *Phys. Rev. B* **76**, 224107 (2007).

[38] E. Mozafari, B. Alling, P. Steneteg, and I. A. Abrikosov, *Phys. Rev. B* **91**, 094101 (2015).

[39] Z. Zhang, H. Li, R. Daniel, C. Mitterer, and G. Dehm, *Phys. Rev. B* **87**, 014104 (2013).

[40] G. Abadias, C.-H. Li, L. Belliard, Q. M. Hu, N. Greeneche, and P. Djemia, *Acta Mater.* **184**, 254 (2020).

[41] A. Herwadkar and W. R. L. Lambrecht, *Phys. Rev. B* **79**, 035125 (2009).

[42] P. Subramanya Herle, M. S. Hegde, N. Y. Vasathacharya, S. Philip, M. V. Rama Rao, and T. Sripathi, *J. Solid State Chem.* **134**, 120 (1997).

[43] S. Kerdongpanya, B. Sun, F. Eriksson, J. Jensen, J. Lu, Y. K. Koh, N. V. Nong, B. Balke, B. Alling, and P. Eklund, *J. Appl. Phys.* **120**, 215103 (2016).

[44] C. X. Quintela, B. Rodríguez-González, and F. Rivadulla, *Appl. Phys. Lett.* **104**, 022103 (2014).

[45] M. A. Gharavi, S. Kerdongpanya, S. Schmidt, F. Eriksson, N. V. Nong, J. Lu, B. Balke, D. Fournier, L. Belliard, A. I. Febvrier, C. Pallier, and P. Eklund, *J. Phys. D: Appl. Phys.* **51**, 355302 (2018).

[46] M. E. McGahay, S. V. Khare, and D. Gall, *Phys. Rev. B* **102**, 235102 (2020).

[47] A. I. Febvrier, N. V. Nong, G. Abadias, and P. Eklund, *Applied Physics Express* **11**, 051003 (2018).

[48] N. A. Muhammed Sabeer and P. P. Pradyumnan, *Materials Science and Engineering: B* **273**, 115428 (2021).

[49] G. Abadias, L. E. Koutsokeras, S. N. Dub, G. N. Tolmachova, A. Debelle, T. Sauvage, and P. Villechaise, *J. Vac. Sci. Technol. A* **28**, 541 (2010).

[50] A. I. Febvrier, J. Jensen, and P. Eklund, *J. Vac. Sci. Technol. A* **35**, 021407 (2017).

[51] B. Bakhit, D. Primetzhofer, E. Pitthan, M. A. Sortica, E. Ntemou, J. Rosen, L. Hultman, I. Petrov, and G. Greczynski, *J. Vac. Sci. Technol. A* **39**, 063408 (2021).

[52] G. Kresse and J. Furthmüller, *Phys. Rev. B* **54**, 11169 (1996).

[53] G. Kresse and J. Furthmüller, *Computational Materials Science* **6**, 15 (1996).

[54] P. E. Blöchl, *Phys. Rev. B* **50**, 17953 (1994).

[55] G. Kresse and D. Joubert, *Phys. Rev. B* **59**, 1758 (1999).

[56] S. L. Dudarev, G. A. Botton, S. Y. Savrasov, C. J. Humphreys, and A. P. Sutton, *Phys. Rev. B* **57**, 1505 (1998).

[57] K. Balasubramanian, S. V. Khare, and D. Gall, *Acta Mater.* **159**, 77 (2018).

[58] P. A. Stampe, M. Bullock, W. P. Tucker, and J. K. Robin, *J. Phys. D: Appl. Phys.* **32**, 1778 (1999).

[59] Z. Hui, X. Tang, R. Wei, L. Hu, J. Yang, H. Luo, J. Dai, W. Song, X. Liu, X. Zhu, and Y. Sun, *RSC Advances* **4**, 12568 (2014).

[60] D. Gall, C.-S. Shin, T. Spila, M. Odén, M. J. H. Senna, J. E. Greene, and I. Petrov, *J. Appl. Phys.* **91**, 3589 (2002).

[61] M. A. Gharavi, G. Greczynski, F. Eriksson, J. Lu, B. Balke, D. Fournier, A. le Febvrier, C. Pallier, and P. Eklund, *J. Mater. Sci.* **54**, 1434 (2019).

[62] M. Magnusson, M. Mattesini, N. V. Nong, P. Eklund, and L. Hultman, *Phys. Rev. B* **85**, 195134 (2012).

[63] L. Chaput, P. Pécheur, J. Tobola, and H. Scherrer, *Phys. Rev. B* **72**, 085126 (2005).

[64] H. I. Yoo, M. W. Barsoum, and T. El-Raghy, *Nature* **407**, 581 (2000).

Supplementary information

P-type behavior of CrN thin films by control of point defects

Arnaud le Febvrier^{1*}, Davide Gambino^{1*}, Fabien Giovannelli², Babak Bakhit¹, Simon Hurand³, Gregory Abadias³, Björn Alling¹, Per Eklund¹

*Corresponding authors: arnaud.lefebvrier@liu.se, davide.gambino@liu.se

Affiliation

¹ *Department of Physics, Chemistry and Biology (IFM), Linköping University, SE-58183 Linköping, Sweden*

² *GREMAN UMR-CNRS 7347, Université de Tours, INSA Centre Val de Loire 15 rue de la chocolaterie, CS 2903, 41029 Blois Cedex, France*

³ *Institut Pprime, Département de Physique et Mécanique des Matériaux, UPR 3346, CNRS-Université de Poitiers-ENSMA, 11 Boulevard Marie et Pierre Curie, - TSA 41123, 86073 Poitiers Cedex 9, France*

I. Elemental composition

Table 1 gives the details of the ToF-ERDA analysis displayed in figure 1 in the main manuscript. The ToF-ERDA analysis has been performed for the films deposited on c-plane sapphire and MgO (100), only.

Table 1: Elemental composition measured by ToF-ERDA for the films deposited on c-plane sapphire and MgO (100) substrate using different N₂% in the gas flow ratio.

Substrate	N ₂ % in the gas flow ratio	ToF-ERDA analysis results						N/Cr		(N+O)/Cr	
		Cr		N		O		Value	Error \pm	Value	Error \pm
		Value (%)	Error \pm (%)	Value (%)	Error \pm (%)	Value (%)	Error \pm (%)				
c-plane sapphire	77	49.6	0.3	49.9	0.5	0.4	0.1	1.01	0.04	1.02	0.04
	68	50.1	0.4	49.5	0.5	0.4	0.1	0.99	0.03	1.00	0.03
	62	50.4	0.4	49.2	0.4	0.4	0.1	0.98	0.03	0.99	0.03
	57	50.8	0.3	48.7	0.3	0.5	0.1	0.97	0.02	0.97	0.02
	51	51.8	0.3	47.8	0.3	0.5	0.1	0.93	0.02	0.93	0.02
	40	59.3	0.3	40.2	0.3	0.5	0.1	0.69	0.02	0.69	0.02
MgO (100)	77	46.8	0.7	52.1	0.8	0.7	0.1	1.11	0.04	1.13	0.07
	68	49.1	0.6	49.8	0.7	0.9	0.1	1.01	0.03	1.03	0.06
	62	50.3	0.7	48.8	0.8	0.6	0.1	0.97	0.03	0.98	0.06
	57	50.2	0.8	49	0.9	0.6	0.1	0.98	0.04	0.99	0.07
	51	54.3	0.7	45	0.8	0.4	0.1	0.83	0.03	0.84	0.05
	40	57.7	0.7	41.2	0.7	0.9	0.1	0.71	0.02	0.73	0.05

Table 2 displays the details of WDS analysis performed on all substrates for the N rich sides of the series. Note here that the differences between ToF-ERDA and WDS could come from the charging effect from the substrates. The trend observed by ToF-ERDA are also observed on WDS within the error bars of the measurement.

Table 2: Elemental composition measured by WDS for the films deposited on c-plane sapphire and MgO (100) substrate using different N₂% in the plasma.

Substrate	N ₂ % in the gas flow ratio	WDS analysis results				N/Cr	
		Cr		N			
		Value (%)	Error ± (%)	Value (%)	Error ± (%)	Value	Error ±
c-plane sapphire	77	48.9	1.0	51.1	1.0	1.04	0.05
	68	47.8	1.0	52.2	1.0	1.09	0.05
	62	47.6	1.0	52.4	1.0	1.10	0.05
	57	47.9	1.0	52.1	1.0	1.09	0.05
	51	-	-	-	-	-	-
	40	-	-	-	-	-	-
MgO (100)	77	48.3	1.0	51.7	1.0	1.07	0.05
	68	48.5	1.0	51.5	1.0	1.06	0.05
	62	48.8	1.0	51.2	1.0	1.05	0.05
	57	51.0	1.0	49.0	1.0	0.96	0.05
	51	-	-	-	-	-	-
	40	-	-	-	-	-	-
LaAlO ₃ (100)	77	46.8	1.0	53.2	1.0	1.11	0.05
	68	47.5	1.0	52.5	1.0	1.05	0.05
	62	48.4	1.0	51.6	1.0	1.07	0.05
	57	50.4	1.0	49.6	1.0	0.98	0.05
	51	-	-	-	-	-	-
	40	-	-	-	-	-	-

II. X-Ray diffraction

Figure S1 shows the full θ - 2θ XRD pattern for the film s deposited on the three different substrates. Only one family of peak of diffraction is observed for the $\text{CrN}_{1-\delta}$ NaCl structure, while Cr_2N appears when the films are deposited with lower content of nitrogen in the plasma, note here that at that scale, the differentiation between Cr_2N and CrN for the films deposited on MgO and LaAlO_3 is difficult. Refer to the main manuscript and figure S2 for a more detailed analysis.

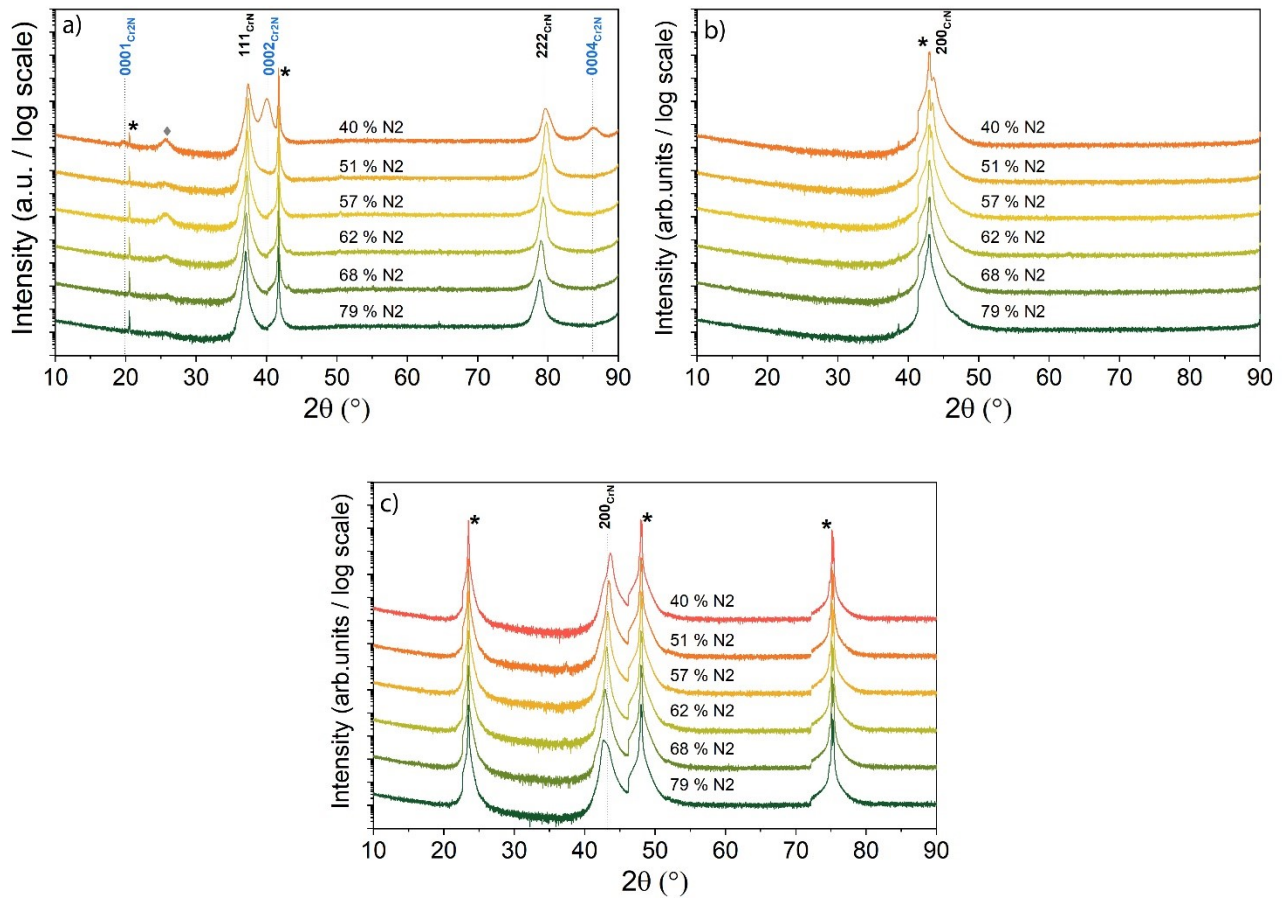


Figure S1: Full range XRD pattern of $\text{CrN}_{1-\delta}$ films deposited using different N₂% in gas flow ratio (from 40 to 77 %) and on a) c-plane Al_2O_3 , b) MgO (100), c) LAO (100). Measurement performed in a Bragg Brentano configuration using a $\text{Cu K}\alpha$ radiation with a nickel filter. Peaks marked with * correspond to the substrate peaks: 0006 (Al_2O_3), 200 (MgO), 200 (LAO)

Figure S2 shows the XRD patterns of the films deposited on MgO (100) under different N₂% in the gas flow ratio. A monochromatic beam CuK_{α1} was used, and the measurement was performed with an 0.1° offset in ω in order to reduce the intensity of the substrate peak and visualize possible overlapping peaks from the film. The observations are similar as the ones on the films deposited on c-plane sapphire (see main manuscript figure 2). Few peaks are observable: i) the substrate peak; ii) the 002 CrN_{1+δ} shifting to higher angle when N₂% reduces and iii) two peaks 1120 and 2020 belonging to Cr₂N. The CrN films deposited at high N₂% are constituted of a phase isotype as the NaCl CrN phase. At lower N₂%, a mixture between cubic CrN and Cr₂N phases is observed. At the lowest N₂% in the gas flow ratio the film is mainly constituted of Cr₂N and CrN as secondary phase.

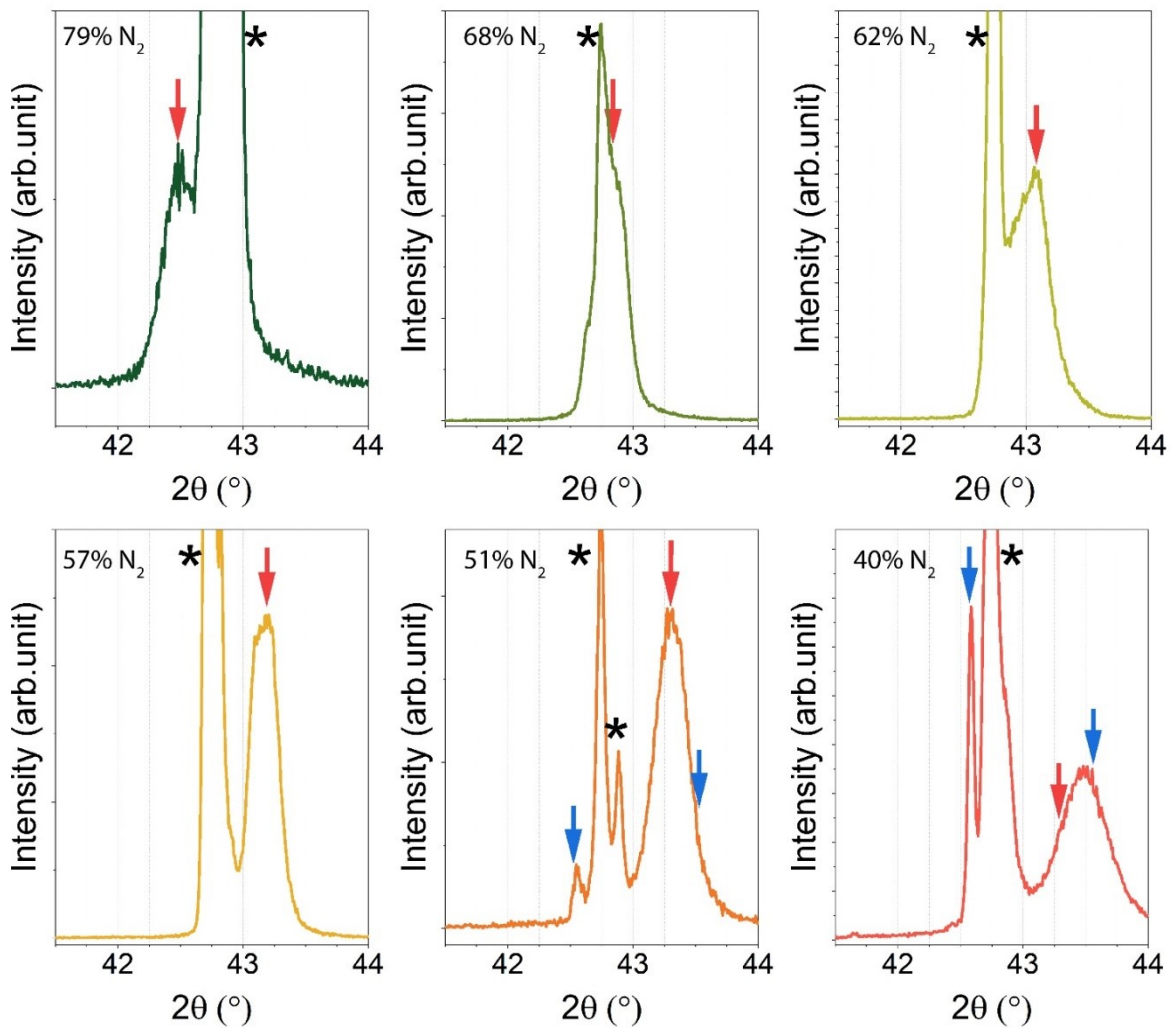


Figure S2: 0-2θ XRD patterns of CrN_{1-δ} films deposited using different N₂% in the gas flow ratio (from 40 to 79 %) and on MgO (100). Measurement were performed using an ω offset of = 0.1° using a Cu K_{α1} radiation. Peaks marked with * correspond to 002 reflection of the MgO substrate, the peaks marked with a red arrow correspond cubic CrN_{1+δ} and those with a blue arrow to Cr₂N.

III. Morphology

Figure S3 display the SEM micrographs of the surface of the $\text{CrN}_{1+\delta}$ films on different substrate and under different $\text{N}_2\%$ in the gas flow ratio. For % higher than 62% of N_2 , the morphology is a typical for a cubic CrN phase grown on c-plane sapphire similar as other nitride (ScN, VN, CrN) on the same substrates. The morphology gradually changes with an increase of the grains size when the $\text{N}_2\%$ in the gas flow ratio reduces. The morphology is identical on both MgO (100) and LAO (100) substrates with a well-defined arrangement of square shaped grains at high $\text{N}_2\%$ gas flow ratio. When the $\text{N}_2\%$ reduces to 57% and 51% the films are constituted of very fine grains with an underlying structure similar to the one observed for the films deposited with higher $\text{N}_2\%$. At the lowest $\text{N}_2\%$ in the gas flow ratio, the film morphology becomes relatively rough with larger grains

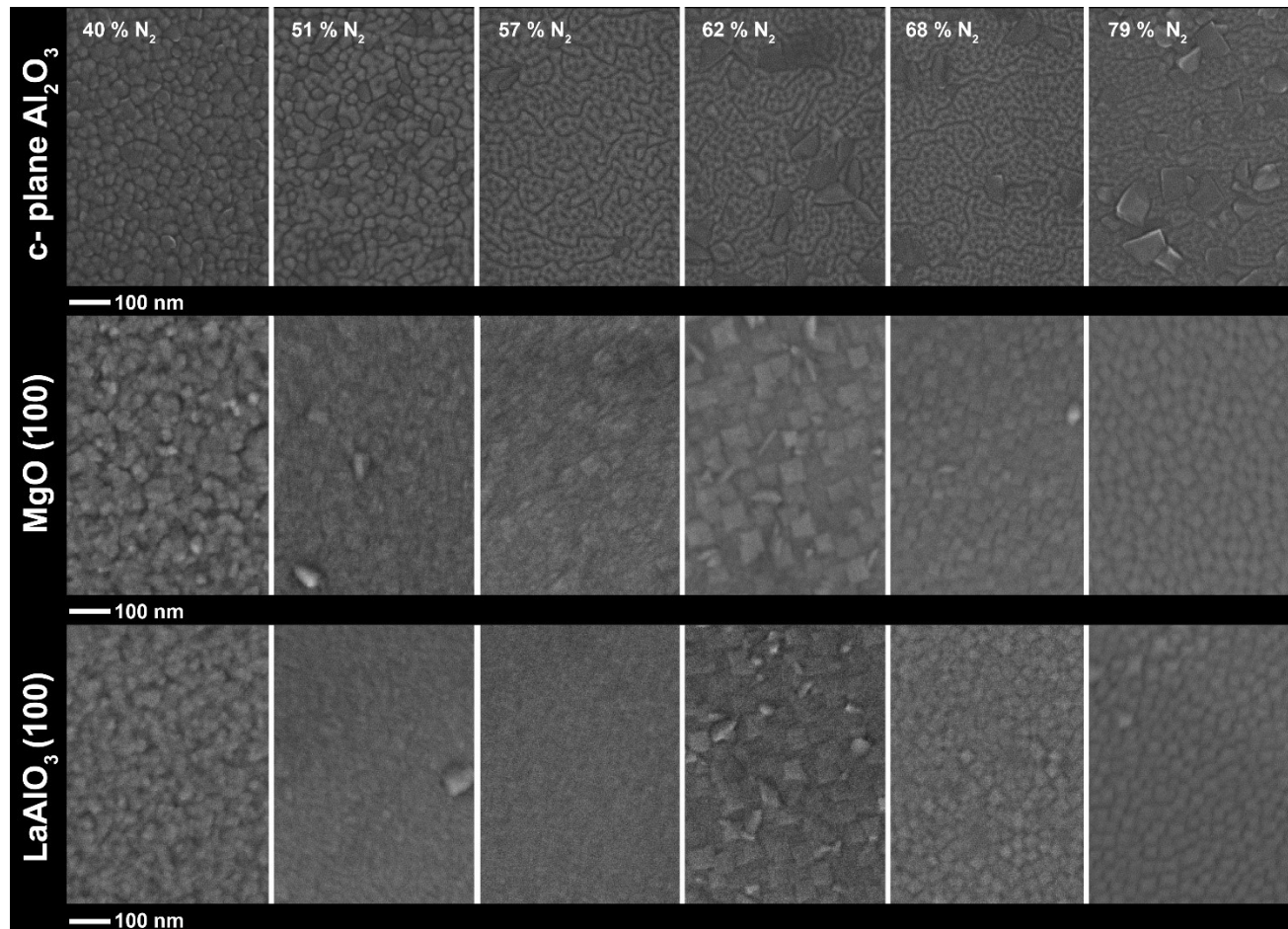


Figure S3: Surface micrographs of the films deposited under different $\text{N}_2\%$ in the gas flow ratio (40%-79%) and on different substrates (c-plane sapphire, MgO (100) and LAO (100))

